Theor Chem Acc (2012) 131:1211
DOI 10.1007/s00214-012-1211-1

REGULAR ARTICLE

Effects of molecular dynamics and solvation on the electronic structure of molecular probes

Pasquale Caruso · Mauro Causà · Paola Cimino · Orlando Crescenzi · Maddalena D'Amore · Roberto Improta · Michele Pavone · Nadia Rega

Received: 28 December 2011 / Accepted: 21 March 2012 / Published online: 10 April 2012

Abstract Most spectroscopic parameters are influenced by nuclear dynamics and by the chemical environment. However, proper inclusion of these effects still represents a challenge in computational spectroscopy studies. In many cases, a route coupling satisfactory accuracy with reasonable computational costs consists in the integration of DFT-based methods to compute spectroscopic parameters, with ab initio molecular dynamics simulations to sample from the classical phase space of the system. Here, we discuss the application of this approach in two case studies of remarkable practical interest, namely the simulation of the absorption spectrum of 9-methyladenine, an adenine nucleoside model; and the prediction of electron spin resonance parameters for nitroxyl radicals, the prototypical spin probes. In both cases, the accuracy of the results increases significantly when the subtle interplay of intramolecular dynamics and solvent effects is introduced.

Keywords Quantum mechanical calculations · Solution · Dynamics · Absorption spectra · EPR spectra · Adenine · Nitroxides · Electron density analysis

Dedicated to Professor Vincenzo Barone and published as part of the special collection of articles celebrating his 60th birthday.

P. Caruso
IIT@CRIB Center for Advanced Biomaterials for Healthcare, Italian Institute of Technology, p.le Tecchio 80, 80125 Napoli, Italy

M. Causà (✉) · O. Crescenzi (✉) · M. D'Amore · M. Pavone · N. Rega
Dipartimento di Chimica "Paolo Corradini", Università Federico II di Napoli, Complesso Monte S. Angelo, via Cintia, 80126 Napoli, Italy
e-mail: mauro.causa@unina.it

O. Crescenzi
e-mail: orlando.crescenzi@unina.it

P. Cimino
Dipartimento di Scienze Farmaceutiche, Università di Salerno, via Ponte don Melillo, 84084 Fisciano, SA, Italy

R. Improta
Istituto di Biostrutture e Bioimmagini, CNR, via Mezzocannone 16, 80134 Napoli, Italy

1 Introduction

Experimental studies on molecular spectroscopy and photophysics have greatly benefited from the recent advances in electronic structure methods [1]. The theoretical development of accurate yet feasible computational approaches and the availability of high-performance computing facilities have provided the chemical community with powerful tools to characterize molecular systems of higher and higher complexity [1]. On the one hand, the successful implementation of new models within the framework of density functional theory (DFT) [2] allows to study molecules of realistic dimensions, up to hundreds of atoms. On the other hand, computational spectroscopy techniques allow to investigate in detail the complex interaction of molecules with external electromagnetic fields (see Ref. [1] and references therein).

However, there is still a significant gap between numerical simulations and laboratory experiments. The most important issues are the inclusion in the electronic structure calculations of the nuclear dynamics (i.e., temperature) and of the chemical environment (e.g., the solvent). In the last decades, many theoretical efforts have been devoted to these topics, and recent extensive reviews cover the main results obtained by time-dependent and time-independent approaches [1].

From a general perspective, the influence of nuclear motion should be taken into account in the computation of essentially all kinds of spectroscopic parameters, even those that do not gauge vibrational structure directly (like IR and Raman). In the case of electronic transitions, for example, molecular vibrations are responsible for the fine structure of UV–vis absorption, fluorescence emission, or electronic circular dichroism spectra via the Franck-Condon selection rules (direct effect) [3]. By contrast, in magnetic resonance spectroscopy, the spectral line shapes are determined by long-time dynamics (e.g., diffusion and rotation of the magnetic molecular probe) rather than molecular motions on short-time scales. However, also in this case, temperature does affect the spectroscopic observables by averaging out the corresponding molecular parameters over the structural fluctuations due to molecular vibrations (indirect effect) [4]. A reliable route to account for this indirect effect is the calculation of the spectroscopic property via vibrational averaging with respect to normal modes, with temperature tuning the population of each mode. The method of choice for computing molecular vibrations is the solution of the nuclear Schrödinger equation. Reliable vibrational frequencies can be obtained in this way, but only with a proper correlation consistent description of the electronic potential energy surface and, possibly, by taking into account anharmonicity [5]. Such time-independent approach is very accurate for semirigid systems because it accounts for the quantum-mechanical nature of nuclear motions; however, the computational burden limits its feasibility.

An alternative approach is represented by the sampling of nuclear motions in the classical phase space via molecular dynamics (MD) techniques [6]. In this case, the spectroscopic property of interest is obtained by extracting a consistent set of configurations from the MD trajectories, and by averaging the molecular parameters computed on each of these frames. This time-dependent approach is quite effective, but once again, its accuracy depends on the description of the potential energy surface governing the MD. In most cases, ab initio MD (AIMD) simulations can be exploited to this purposes: thanks to the Car-Parrinello scheme [7, 8], the forces governing nuclear dynamics can be efficiently computed from first principles, within the framework of the density functional theory. From a practical point of view, it is also remarkable that time-dependent approaches allow the use of different levels of theory for the generation of trajectories and for the computation of spectroscopic observables on a subset of the sampled structures. For example, much better statistics can be obtained by MD simulations using reliable semi-empirical force fields, when these are available [6].

In the present study, we explore the performances of dynamical approaches to include nuclear and environmental effects by discussing two case studies: the simulation of the absorption spectrum of an adenine nucleoside model (9-methyladenine, henceforth 9-Me-Ade) in the gas phase and in aqueous solution, and the calculation of electron spin resonance (ESR) parameters for important spin probes such as nitroxyl radicals. As shown below, in both cases, the accuracy of the results considerably increases when the subtle interplay of intra-molecular dynamics and solvent effects is properly accounted for in the electronic structure calculations.

Besides their methodological interest, our results will provide additional insights into two topics of general chemical and biological interest, namely the photophysics of DNA components and the spectroscopic features of some prototypical 'spin labels'/'spin probes'.

The interaction between UV–visible radiation and nucleic acids is a topic of great biological relevance, since it can trigger a cascade a photochemical events leading to mutagenesis. This has motivated, in the last decade, a large number of theoretical and computational studies on the excited state properties of DNA and of its constituent nucleobases [9–13].

Concerning isolated nucleobases, time-resolved experiments evidenced very short (sub-ps) lifetimes of the lowest energy bright singlet excited states that have been rationalized by quantum mechanical calculations [9, 13]. For all the nucleobases, barrier-less paths exist for the spectroscopic states, connecting the Franck-Condon (FC) region with a conical intersection (CI) with the ground electronic state (S_0). However, several interesting features have not been assessed yet, as for example the involvement of dark excited states in the decay process [10, 13].

While for uracil derivatives, experiments and calculations both showed that a part of the population of the lowest energy bright excited state (with $\pi \rightarrow \pi^*$ character) can decay to a close lying $n\pi^*$ state [13, 14], the participation of dark excited states to the photophysics of adenine is still a matter of debate [15, 16].

As a first step toward the complete understanding of the factors ruling the interplay between bright and dark excited states in adenine derivatives, here we have computed the absorption spectra of 9-Me-Ade in the gas phase and in aqueous solution by exploiting a dynamical approach (vide infra). We focus our attention on the effects of intra-molecular vibrational motion on the electronic spectrum and on the coupling among the different excited states. For the adenine derivative in aqueous solution, we mainly address here bulk solvent effects, while a detailed treatment of hydrogen bonding interactions will be tackled in a forthcoming paper.

The second case study concerns an ESR observable, namely the nitrogen hyperfine coupling constant (a_N), for nitroxide free radicals. Nitroxides are characterized by a

long-living spin-unpaired electronic ground state and by molecular properties strongly dependent on the chemical environment embedding the NO moiety. These features led to such a widespread application of nitroxide derivatives as spin labels, spin probes, redox probes, or contrast agents that it is quite difficult to overemphasize the relevance of this class of compounds in many fields of modern chemistry [17]. In particular, we will focus on two of the nitroxide radicals most exploited in spin-probe/label ESR experiments, namely (2,2,6,6-tetramethylpiperidin-1-yl)oxidanyl (TEMPO) and (2,2,5,5-tetramethylpyrrolidin-1-yl)oxidanyl (PROXYL).

The molecular properties of these nitroxides strongly depend on the chemical environment, and recent theoretical simulations have achieved a detailed characterization of such dependencies for isotropic solutions in non-polar/polar and protic/aprotic solvents [18–22]. Besides the effects of complex chemical environment, ESR parameters are also affected by intra-molecular dynamics.

Here, we discuss the effects of intra-molecular dynamics on the a_N value of two different nitroxides that have a five-atom- (PROXYL) and six-atom- (TEMPO) ring backbone. In particular, we focus our analysis on the flexibility of the nitroxide moiety and its role in tuning the ESR observable. To this aim, we performed a characterization of minimum-energy structures, a rigid scan of the PES, and ab initio molecular dynamics simulations for both PROXYL and TEMPO in the gas phase. It has been recently demonstrated for these radicals that the AIMD-based time-dependent approach is in full agreement with the aforementioned time-independent approach [23]. In order to gain further chemical information, we also report a topological analysis of the nitroxide electronic structure by means of the maximum probability domains (MPD) approach [24, 25], which has allowed us to identify and discuss the subtle variations of the electron density with respect to structural fluctuations.

2 Methods

2.1 Time-dependent approach to the computation of optical and EPR spectra

Countours of optical spectroscopic bands can be obtained from a classical treatment of nuclear motion. In the classical limit, the absorption cross section can be expressed as

$$c\sigma(\omega) = \frac{4\pi\omega}{3}\int \rho_g(Q)|\mu_{ge}(Q)|^2\delta(V_g + \omega - V_e)dQ \qquad (1)$$

where $\rho_g(Q)$ is the classical density of normal coordinates Q in the ground state, μ_{ge} is the transition dipole between the ground and the excited state, δ is the Dirac delta, and $V_{g(e)}$ is the energy potential in the ground (excited) state. Therefore, absorption band shapes can be retrieved by a configurational sampling in the classical phase space of the electronic ground state, along with the corresponding transition dipole and vertical transition energy. While in this classical approach, the details of vibrational progression are lost, finite temperature effects in complex environment (solvent) can be easily taken into account by analysis of molecular dynamics trajectories. In this work, absorption spectra are constructed by means of a posteriori time-dependent DFT analysis of ab initio dynamics.

Classical sampling can also be exploited to introduce finite temperature effects on spectroscopic parameters. In the present work, we focus on the nitrogen EPR hyperfine coupling constant (a_α), which has been computed according to the following expression:

$$a_\alpha = \frac{8}{3}\pi g_\alpha g_e \mu_\alpha \mu_e \rho_s(r_\alpha) \qquad (2)$$

where μ_α and g_α are, respectively the magneton and the g factor of nucleus α, μ_e is the Bohr magneton, g_e is the g value for the electron, and $\rho_s(r_\alpha)$ is the electron spin density at the α nuclear position [4].

2.2 Maximum probability domains analysis on nitroxide probes

To exhaustively analyze the chemical bonding in open-shell nitroxyl systems, we resorted both to electron localization function [26] (ELF) and the maximum probability domains (MPDs) [24, 25]. In MPDs analysis, our first objective has been to identify spatial subsystems $\Omega \subset R^3$ in the nitroxide electronic system by specifying a given electron number v; we chose $v = 2$, 1 when trying to find by our calculations an electron pair and an unpaired electron, respectively. The next choice is the arbitrary definition of a volume Ω where we are going to find a given number of electrons v with a certain probability p; in essence, this definition reflects the quantum-mechanical view that, for a given state Ψ, the occurrence of a certain number of electrons v in Ω can only be formulated in terms of probability. Thus, we compute the probability of finding exactly v electrons in Ω based on Hartree-Fock wavefunctions and define the regions of space for which the probability to find v electrons becomes a maximum. Finally, for each given value of v, the shape of Ω (now more appropriately indicated as Ω_v) was optimized to find out local maxima of a certain probability by making use of shape derivatives [27]. As in all distributions, information about the probability distribution $p_{(0)}(\Omega), p_{(1)}(\Omega), p_{(2)}(\Omega), \ldots p_{(N)}(\Omega)$ is obtained by means of some parameters: among others, we focused on the mean $\langle N \rangle$. For an N-electrons system, the average number of electrons in Ω is given by:

$$\langle N\rangle(\Omega) = \sum_{v=0}^{N} v p_v(\Omega) \tag{3}$$

This has been obtained by integrating the electron density (ρ) over the domain, as indicated in the following equation:

$$\int_{\Omega} \rho(r) d^3 r = \int_{\Omega} \langle \Psi | \hat{\rho}(r) | \Psi \rangle d^3 r = \langle \Psi | \int_{\Omega} \hat{\rho}(r) d^3 r | \Psi \rangle. \tag{4}$$

2.3 Computational details

Most of the calculations discussed in the present study were performed at the PBE0 level of theory. PBE0 [28] is an hybrid functional in which the spurious self-interaction is partly cured by mixing PBE and Hartree-Fock exchange with amounts determined in order to fulfill a number of physical conditions, without resorting to any fitting procedure [28]. In particular, PBE0 obeys both the Levy condition [29] and the Lieb-Oxford bound [30], providing a fairly accurate description of the low-density/high-gradient regions.

Regarding 9-Me-Ade, geometries were provided by PBE0/6-31G(d) optimizations in both the gas phase and the aqueous solvent, by means of the polarizable continuum model (PCM) [31–33]. Since the presence of explicit solute–solvent hydrogen bonds is particularly important for the excited states with $n \rightarrow \pi^*$ character, we have also performed test calculations by studying the model depicted in Fig. 1, which includes 4 water molecules of the first solvation shell. The excited state vertical excitation energies (VEE) have been computed at the TD-PBE0 level, by using standard 6-31G(d), 6-31+G(d,p), and 6-311+G(2d,2p) basis sets.

AIMD simulations were performed in both the gas phase and aqueous solvent within the atom-centered density matrix propagation (ADMP) MD scheme [34–37], which allows to use the most accurate hybrid HF-DFT levels of theory [38]. Bulk solvent effects were accounted for by the PCM, and explicit solute–solvent interactions were not included in ADMP dynamics runs nor in spectra calculations, since such more detailed treatment was deemed to fall outside the explorative purposes of the present study.

The configurational space accessible in the ground state was sampled by ADMP trajectories obtained at the B3LYP/6-31G(d,p) and B3LYP/6-31G(d,p)/CPCM levels of theory for the gas phase and the aqueous solution, respectively. After 5 ps of equilibration, trajectories have been collected for about 10 ps, with a time step of 0.2 fs. The fictitious value of the electronic mass was set to 0.5 amu bohr^2, and a velocity rescaling procedure maintained the average value of the total kinetic energy corresponding to a temperature of 300 K.

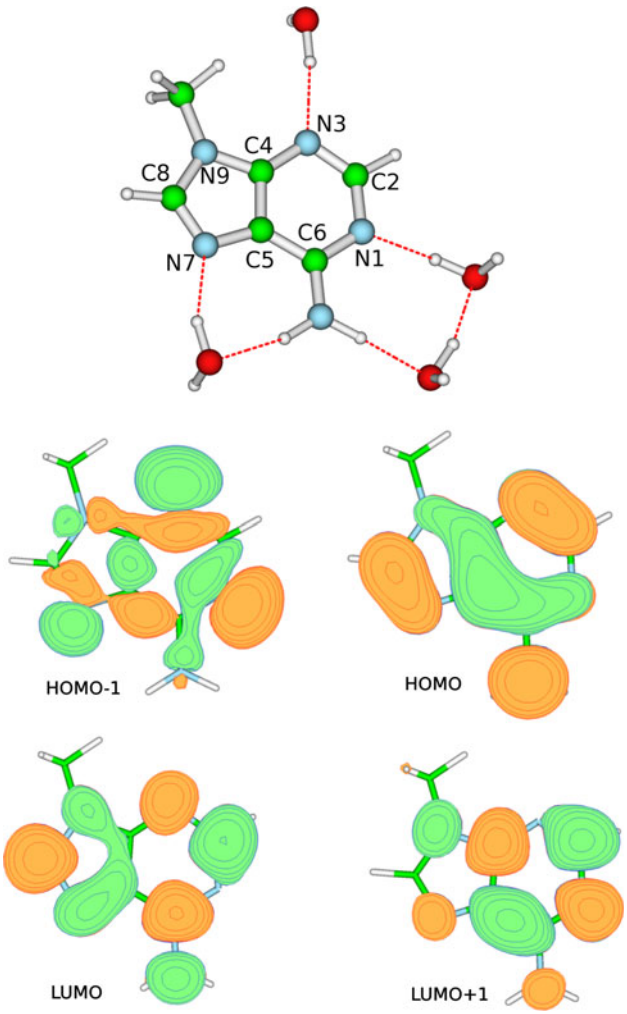

Fig. 1 Schematic drawings of 9-methyladenine and of its frontier orbitals

A number of configurations (approximatively 2000) uniformly extracted from the ADMP trajectories have been considered to compute excited state VEEs at the TD-PBE0/6-31+G(d,p) and TD-PBE0/6-31+G(d,p)/CPCM levels of theory. In order to evaluate direct and indirect bulk solvent effects on the electronic transitions, we considered gas phase VEE calculations on samplings obtained in both the gas phase and aqueous solution. To produce graphs of the absorption spectra, each transition was convoluted by a gaussian with FWHM = 0.05 eV, by a procedure similar to that adopted by Thiel and coll [39].

All the calculations carried out on the TEMPO and PROXYL nitroxide radicals were performed using the PBE0 density functional in combination with the polarized double-ζ basis set N07D [40], purposely tailored for DFT-based calculations of magnetic parameters [41, 42]. Gas phase minimum-energy structures were optimized using tight criteria of convergence. From the minima, we performed a rigid scan of the NO out-of-plane dihedral angle

(vide infra). ADMP simulations were performed in the gas phase with a time step of 0.2 fs, for a trajectory of ~ 15 and ~ 18 ps in the case of PROXYL and TEMPO, respectively. The electron fictitious mass parameter was set to 0.5 amu bohr^2. The translational motion and the total angular momentum were projected out at each time step, while an average temperature of 298 K was pursued via rescaling of nuclei velocity modulus. For both PROXYL and TEMPO, the hyperfine constant a_N has been computed on minima, along the rigid scan and along the AIMD trajectories.

All the calculations were carried out by using a development version of the Gaussian package [43]. A 3D extension of MPDs [24, 25] analysis implemented in a development version of CRYSTAL code [44], able to deal both with molecules and crystalline systems in the Hartree-Fock and DFT approximation, has been adopted. The code has been modified by considering spins separately, and for the first time, we apply the method to wave functions obtained from unrestricted Hartree-Fock calculations.

3 Results and discussion

3.1 Solvent effect on the absorption spectra of 9-methyladenine

As anticipated in the introduction, for adenine several studies interpreted the very short excited state lifetime, in aqueous solution [45, 46] and the gas phase [47, 48], as an ultrafast radiation-less decay of the spectroscopic bright state (L_a, see below) to S_0 ($L_a \rightarrow S_0$) [15, 49]. On the other hand, recent studies suggested that L_a is strongly mixed in the FC region with a close lying dark $n\pi^*$ state and that ground state recovery follows a different pathway, passing through the dark $n\pi^*$ state ($L_a \rightarrow n\pi^* \rightarrow S_0$) [15, 49]. Interestingly, the same mechanism has been proposed to be active also for Ade bases within DNA [16].

It is clear that a key factor modulating the relative importance of the two different pathways is the mixing between the different excited states in the FC region: since a barrier-less path on the L_a surface connects the FC region with a CI with S_0, only an ultrafast $L_a \rightarrow n\pi^*$ decay would be competitive with the direct $L_a \rightarrow S_0$ decay. Intramolecular vibrational motion, distorting the planar geometry of the purine ring and potentially coupling L_a and $n\pi^*$, could play a crucial role. As a consequence, we have decided to investigate the effect of nuclear motion on the absorption spectrum of 9-Me-Ade.

Solvent effects are also expected to be important because they can influence the $L_a \rightarrow n\pi^*$ interplay directly, by affecting the energy of the different electronic transitions, or indirectly, by changing the equilibrium geometry and vibrational properties of adenine.

The vertical excitation energies (v_A) of 9-methyladenine in the gas phase and in aqueous solution are reported in Table 1. Confirming the results of the previous computational studies [15, 39], three electronic transitions contribute to the lowest energy absorption band: two with

Table 1 Vertical excitation energies (in eV) computed for 9-Me-Ade and the 9-Me-Ade$(H_2O)_4$ water cluster in the gas phase (TD-PBE0) and in aqueous solution (TD-PBE0/PCM)

	TD/PBE0			TD-PBE0/PCM	
	9-Me-Ade[a]	9-Me-Ade[b]	9-Me-Ade$(H_2O)_4^b$	9-Me-Ade[a]	9-Me-Ade$(H_2O)_4^b$
6-31G(d)					
$Sn\pi$	5.18 (0.007)	5.14 (0.003)	5.10 (0.000)	5.27 (0.020)	5.63 (0.001)
L_a	5.26 (0.194)	5.28 (0.185)	5.26 (0.210)	5.21 (0.223)	5.10 (0.245)
L_b	5.49 (0.050)	5.45 (0.060)	5.48 (0.040)	5.42 (0.072)	5.37 (0.120)
6-31+G(d,p)					
$Sn\pi$	5.15 (0.013)	5.10 (0.096)	5.07 (0.05)	5.27 (0.002)	5.60 (0.000)
L_a	5.09 (0.222)	5.13 (0.140)	5.08 (0.237)	5.08 (0.295)	4.98 (0.305)
L_b	5.39 (0.028)	5.36 (0.028)	5.39 (0.022)	5.32 (0.045)	5.26 (0.087)
6-311+G(2d,2p)					
$Sn\pi$	5.13 (0.006)	5.10 (0.037)	5.04 (0.06)	5.26 (0.002)	5.57 (0.000)
L_a	5.03 (0.225)	5.05 (0.195)	5.02 (0.229)	5.02 (0.292)	4.92 (0.300)
L_b	5.33 (0.024)	5.30 (0.021)	5.32 (0.010)	5.26 (0.038)	5.20 (0.078)

Geometries were obtained by PBE0/6-31G(d) and PBE0/6-31G(d)/PCM optimizations. Oscillator strengths are given in parentheses

Experimental band maximum: dA 4.77 eV [60]; adenine in the gas phase at the TD-PBE0/6-31+G(d,p)//PBE0/6-31G(d) level of theory: $Sn\pi$ 5.13(0.018), L_a 5.19(0.219), L_b 5.42(0.033)

[a] Gas phase optimization

[b] Aqueous solvent optimization

$\pi \rightarrow \pi^*$ character (usually labeled $^1\pi^* L_a$ and $^1\pi^* L_b$, respectively, hereafter simply L_a and L_b) and one with $n \rightarrow \pi^*$ character (hereafter $Sn\pi$). All the methods agree in predicting that $S_0 \rightarrow L_a$ is the most intense transition: it can be described as a HOMO $\rightarrow$ LUMO excitation. The L_b state corresponds mainly to a HOMO $\rightarrow$ LUMO+1 $\pi \rightarrow \pi^*$ transition. $Sn\pi$ can be described as HOMO-1 $\rightarrow$ LUMO transition, involving the transfer of an electron from a non bonding Kohn-Sham (KS) orbital (HOMO-1 in Fig. 1) to the $^1\pi^*$ orbital.

The prediction of TD/PBE0 calculations [50, 51] is consistent with those of the most accurate ab initio methods [15, 39]. As reported in the Notes of Table 1, for adenine in the gas phase (the system most thoroughly studied), we predict that $Sn\pi$ corresponds to the lowest energy excited states at the FC point, being $\sim$0.1 eV more stable than L_a. In the literature, there is more disagreement concerning the relative energy of the L_a and L_b transitions: while according to some studies, L_b is slightly more stable than L_a [15, 52, 53], our calculations and other computational studies [39] predict that L_b is $\sim$0.2 eV less stable than L_a. In any case, L_b should not be significantly involved in the excited state decay of adenine derivatives [49, 52–54].

As shown in Table 1, the 9-methyl substituent and, especially, the inclusion of solvent effects strongly favor L_a over $Sn\pi$. When only bulk solvent effects are included by PCM, for 9-Me-Ade L_a corresponds to S_1, being more stable than $Sn\pi$ by 0.05–0.2 eV (an increase in the size of the basis set favors L_a). The most significant consequence of the presence of solute/solvent hydrogen bonds (9-Me-Ade · 4 H_2O model) is the destabilization of the $n \rightarrow \pi^*$ transition by $\sim$0.3 eV. In analogy with what found in uracil-like molecules [55], this latter kind of transitions is blue-shifted in the presence of hydrogen bonds with the solvent molecules. The transfer of an electron from the nitrogen lone pair (acting as donor in the hydrogen bonds with water molecules) to a $^1\pi^*$ orbital delocalized on the ring decreases the strength of the solute–solvent interactions.

From the quantitative point of view, our results are in very good agreement with experiments. For the 9-Me-Ade · 4 H_2O model, the computed v_a is blue-shifted by only 0.2 eV with respect to the maximum of the absorption band of Adenosine in solution. Furthermore, we predict a solvent red-shift in the range 0.10–0.16 eV (depending on the basis set), the corresponding experimental estimate being 0.15 eV (see Ref. [39] and references therein). For what concerns the main purpose of this study, the coupling between L_a and $Sn\pi$ is always rather small. The contributions of the HOMO $\rightarrow$ LUMO excitation to $Sn\pi$ and, conversely, that of the HOMO-1 $\rightarrow$ LUMO excitation to L_a are always smaller than 0.2. Furthermore, also when L_a and $Sn\pi$ v_A are within 0.05 eV, the L_a oscillator strength is always at least ten times that of $Sn\pi$: a strong coupling between the two states would have instead produced a much larger intensity borrowing between the two states.

Before analyzing the spectra computed from our ADMP/PBE0//TD-PBE0 procedure, it is important to remind that, especially in the presence of a strong vibronic coupling between L_a and $Sn\pi$, our approach is not expected to provide an accurate description of the absorption lineshape, which would require a quantum-mechanical treatment [56, 57] of nuclear dynamics. However, we can provide qualitative insights on the role of intramolecular vibrations in promoting the L_a and $Sn\pi$ coupling. In this spirit, without resorting to a detailed diabatization procedure, we shall use the ratio (r) between the oscillator strengths of the 'dark' and the 'bright' adiabatic excited states as a qualitative measure of the coupling between L_a and $Sn\pi$ diabatic states. For 9-Me-Ade geometries close to planarity (as in the PBE0 equilibrium minimum) L_a bears indeed all the oscillator strength (the L_b contribution is small) while $Sn\pi$ is almost dark. On the contrary, a coupling between L_a and $Sn\pi$ will be mirrored by a transfer of oscillator strength between the two lowest adiabatic excited states.

Inspection of Fig. 2 shows that in the gas phase, the curve associated withS_1 and S_2 has comparable intensities, the former being only 30 % less intense than the latter. This picture is very different with respect to that reported in Table 1: at the same level of theory, S_1 (in this case almost coinciding with the $Sn\pi$ diabatic state) is a hundred times less intense than S_2 (corresponding to L_a). Actually, the similar intensities of the S_1 and S_2 absorption bands are not only due to the $L_a/Sn\pi$ vibronic coupling. For several geometries, it depends simply on the interchange between L_a and $Sn\pi$ energy, that is L_a corresponds to S_1 and $Sn\pi$ to S_2, without a significant mixing between the two adiabatic states. A preliminary analysis indicates that only in $\sim$50 % of the geometries considered r is $\geq$ 0.1 (moderate coupling), in $\sim$30 % r is $\geq$ 0.3, and only in $\sim$15 % r is $\geq$ 0.5 (strong coupling).

When bulk solvent effects are included in our analysis (middle panel of Fig. 2), the picture is more similar to that provided by the spectrum computed in the S_0 minimum (Table 1). Most of the oscillator strength is carried by S_1, the intensity of the S_2 band being $\sim$40 % of the S_1 one. However, our analysis shows a distribution of the computed r values similar to that found in the gas phase. In other words, inclusion of bulk solvent effects does not seem to dramatically affect the $L_a/Sn\pi$ coupling. In order to further check this conclusion, we have computed the spectra in the gas phase by using the geometries provided by PCM/ADMP calculations (dashed lines in the top panel of Fig. 2). The computed spectra are very similar to those analyzed above. Interestingly, the use of the PCM sampling leads to a slightly larger coupling, in line with results

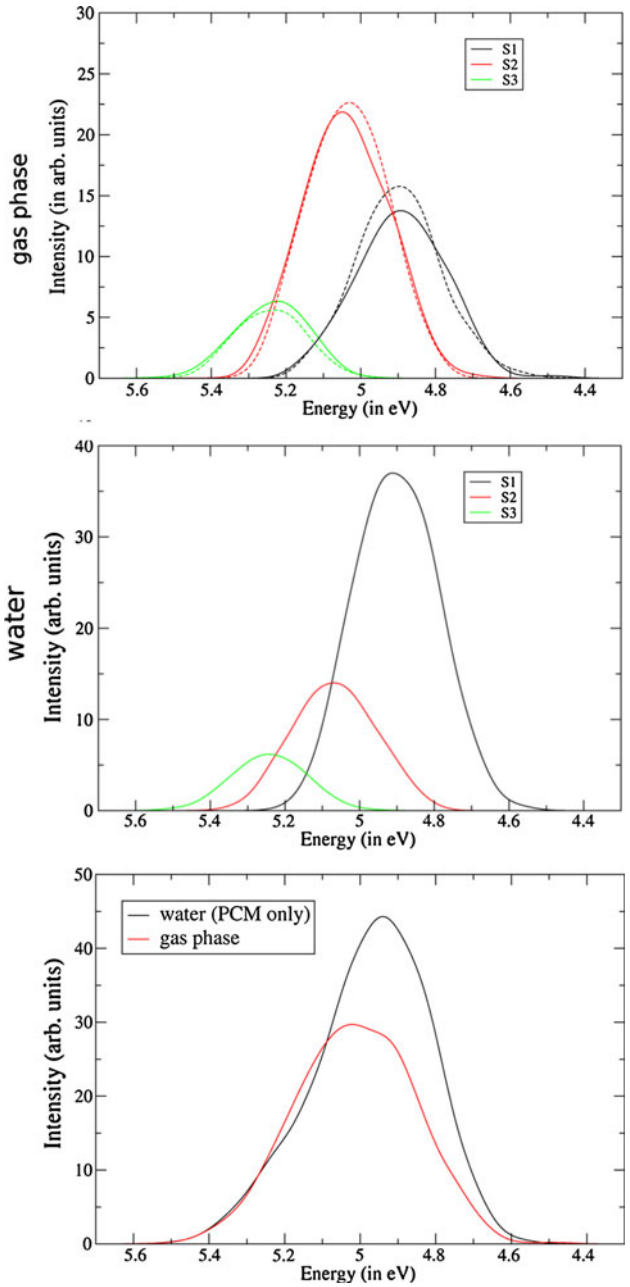

Fig. 2 Absorption bands associated with the three lowest adiabatic excited states for 9-Me-Ade in the gas phase (*upper panel*; the *dashed curves* display the results obtained by using the geometries issuing from ADMP simulations performed in water) and in aqueous solution (*middle panel*), computed by using the TD-PBEO/6-31+G(d,p)//ADMP/PBE0/6-31G(d) procedure described in the text. The resulting absorption spectra are shown in the *bottom panel*

obtained by computing the TD-PBE0 v_A in the gas phase on the geometries optimized in aqueous solution (see the first 2 columns of Table 1).

A detailed characterization of vibronic effects on 9-Me-Ade absorption spectrum in water is outside the scope of the present paper, and, in our case, the absence of explicit solute–solvent interactions could bias the quantitative reliability of our conclusion. A preliminary analysis indicates that, not surprisingly, the out-of-plane motion of the purine nitrogen atoms (whose lone pairs are involved in the $Sn\pi$ excitation) can act as very effective coupling modes. In order to get additional insights, we have extracted and examined more carefully the 10 structures exhibiting the largest r values ($r \geq 0.9$). Our analysis indicates that small departures from planarity (<5°) are sufficient to induce a significant coupling between L_a and $Sn\pi$ states and that the combination of different collective low-frequency torsional mode, not necessarily involving nitrogen atoms, can affect the vibronic coupling. For example, in several structures, the largest deviation from the molecular plane occurs at the C6 position (i.e., the site bearing the amino-substituent, see Fig. 1). In other cases, the coupling is mainly due to the 'bending' of the angle between the 5- and the 6-membered rings (the two rings remaining essentially close to planarity). Finally, pyramidalization of the C2 and C8 carbon atoms can also increase the $L_a/Sn\pi$ coupling.

It is worth noting that our calculations (bottom panel of Fig. 2) predict a noticeable solvent red-shift ($\sim$0.1 eV). The computed value is slightly underestimated with respect to the experimental one, but we recall that at this stage of the analysis, we are not considering explicit solute–solvent interactions; as shown in Table 1, these lead to an additional red-shift of the L_a band in water with respect to the gas phase.

Our picture is globally rather similar to that obtained by Thiel and coll. [39], which points out to a very strong mixing between $Sn\pi$ and L_a states in the FC region; However, a more detailed comparison is not easy, since only 10 optimized snapshot geometries were reported [39]. The simulated absorption spectrum in solution [39] confirms that both the S_1 and S_2 adiabatic states contribute to the lowest absorption band, carrying similar intensities. The ratio between the bands associated with S_1 and S_2 is rather similar to what we found in the gas phase, despite the fact that solute–solvent hydrogen bond interactions were explicitly included in the aforementioned computations [39]. In this respect, it is important to remind that the results reported in Ref. [39] concern adenine, while we have shown the methyl substitution affects the relative energies of L_a and $Sn\pi$ states, favoring the former by $\sim$0.1 eV. Therefore, we can expect that for 9-Me-Ade in a larger fraction of the sampled geometries, L_a would correspond to S_1 and $Sn\pi$ to S_2.

3.2 Dynamical effects on EPR parameters and maximum probability domains of nitroxyl radicals

The molecular structures of TEMPO and PROXYL radicals are shown in Fig. 3. The isotropic hyperfine coupling

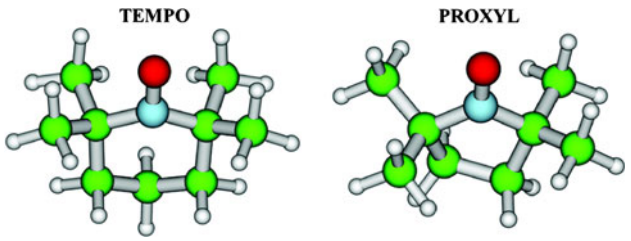

Fig. 3 Molecular structure of the TEMPO (**a**) and PROXYL (**b**) nitroxide radicals; the *white*, *green*, *light-blue* and *red spheres* represent hydrogen, carbon, nitrogen and oxygen atoms, respectively

is a direct measure of the coupling between the spin-unpaired electron and the magnetic moment of a specific nucleus. For nitroxide spin-label or spin-probe experiments, the quantity of interest is the nitrogen hyperfine coupling constant (a_N). For this ESR observable, the most relevant structural parameter of the nitroxide moiety is the NO out-of-plane angle (i.e., the C–N–O…C improper dihedral angle) [18–20]. Due to their cyclic backbone, TEMPO and PROXYL display different minimum-energy conformations in the gas phase, as listed in Table 2. In the case of PROXYL, the five-atom ring leads to a planar conformation of the NO moiety (the oxygen atom lies in the plane defined by the C–N–C atoms). The six-atom ring of TEMPO leads to a nonplanar nitroxide moiety, the oxygen center lying 20° off the C–N–C plane. As a direct consequence of that, the NO bond length in TEMPO is slightly longer than in PROXYL. As a matter of facts, in the planar NO moiety of PROXYL, both the N and O atoms show formal sp^2 hybridization, whereas in the non-planar case of TEMPO, the N hybridization is close to sp^3, leading to an elongation of the NO equilibrium bond length. Table 2 also lists the a_N values computed on the minimum-energy configurations, which are different for the two nitroxides (11.8 and 14.8 Gauss for PROXYL and TEMPO, respectively). Such values can be directly compared to the experimental a_N measured in solution of a non-polar and aprotic solvent with very low dielectric constant, like, for example, dodecane or cyclohexane. The experimental a_N for PROXYL and TEMPO are 14.02 and 15.28 Gauss, respectively [58, 59]. The predicted a_N for the TEMPO minimum-energy structure is more accurate than the one of PROXYL, which is off by 2 Gauss. Part of this discrepancy is due to vibrational averaging. Therefore, a_N was computed on frames extracted along the AIMD trajectories at regular 25-fs intervals for a total of ~500 frames and ~600 frames in the case of PROXYL and TEMPO, respectively. In both cases, the first 3 ps of the AIMD simulations were taken as an equilibration phase and were discarded: this sampling scheme ensures well-converged average values of the magnetic parameters [23]. Table 2 lists structural and a_N values averaged over the AIMD trajectories for both PROXYL and TEMPO.

Clearly, the most significant discrepancy between 'static' and 'dynamic' pictures concerns the out-of-plane bending of the NO moiety, which, judging by the standard deviations, gives rise to large-amplitude motions. The average value corresponds to a planar configuration for both PROXYL and TEMPO. However, by taking the absolute values of the C–N–O–C improper dihedral angle, the averages are now pointing to a pyramidal configuration for both nitroxides. In other words, the NO moieties of both PROXYL and TEMPO oscillate between positive and negative values that are almost equivalent with respect to the pseudo-symmetric C–N–C plane.

Despite the large standard deviation of 2 Gauss, the a_N values averaged over the AIMD trajectories (14 and 15 Gauss for PROXYL and TEMPO, respectively) agree remarkably well with the experimental counterparts. Moreover, in the case of TEMPO, the AIMD average value is very close to that obtained from the minimum-energy structure, while for the PROXYL radical, the proper treatment of temperature and vibrational motions leads to an a_N value that is substantially different from the minimum-energy one. This behavior can be rationalized by considering how the a_N value changes along the out-of-plane bending of the NO moiety, as shown in Fig. 4. As found from geometry optimization, PROXYL shows a minimum at the planar configuration. In the case of TEMPO, the scan of the potential energy surface clearly shows a non-planar minimum-energy structure, the planar configuration being a transition state, even though the barrier is quite low (~2 kcal/mol). Despite this difference in energy profiles, the a_N values of both nitroxides display a

Table 2 Structural and magnetic parameters of TEMPO and PROXYL radicals

	$\text{TEMPO}_{\text{min}}$	$\text{TEMPO}_{\langle ADMP \rangle}$	$\text{PROXYL}_{\text{min}}$	$\text{PROXYL}_{\langle ADMP \rangle}$
N–O	1.269	1.27 (0.02)	1.260	1.27 (0.02)
C–N–O–C (α)	21.4	0 (20)	0.0	0 (16)
$\langle \lvert\alpha\rvert \rangle$		16 (10)		12 (10)
a_N	14.8	15 (3)	11.8	14 (2)

Bond lengths in Angstroms, improper dihedral angles in degrees and nitrogen hyperfine coupling constants (a_N) in Gauss. Standard deviations in parentheses

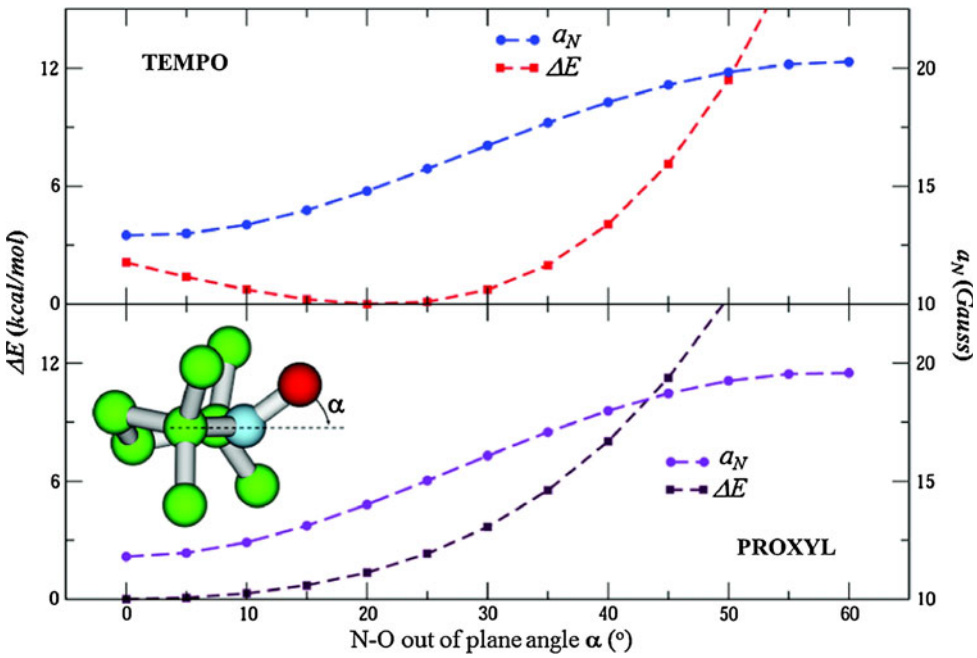

Fig. 4 Energy and a_N changes along the out-of-plane bending of the NO moiety for the TEMPO (*upper panel*) and PROXYL (*lower panel*) nitroxide radicals

very similar trend, from both the quantitative and qualitative points of view. These results highlight the importance of taking properly into account this motion for predicting reliable isotropic hyperfine couplings of nitroxide spin probes.

To better analyze the electronic structure of the nitroxide moiety, we performed a topological study of the PROXYL electron density by means of the ELF and the MPD schemes. Figure 5 depicts the results of both approaches on the nitroxide moiety of the PROXYL minimum-energy planar structure. The ELF core basins can be easily located close to the N and C centers. The oxygen core basin is hidden by lone pairs. The C–N bond is polarized toward the more electronegative nitrogen atom; the very small N–O basin suggests a lower localization of electrons, consistently with the expected multiple nature of the N–O bond. However, the ELF results also show two additional lone pairs around the N center, a quite unexpected location for electrons. In other words, the ELF analysis of the planar PROXYL minimum provides a chemically unsound picture, in which the N center has three σ bonds and two lone pairs. On the contrary, the MPD analysis agrees nicely with chemical common sense. The $\langle N \rangle$ values computed according to Eq. (2) are listed in Table 3. The picture that emerges is in agreement with the chemical imagine of a planar nitroxide structure, with a N=O double bond, two lone pairs on oxygen, and the unpaired electron delocalized on the NO bond. The sum of $\langle N \rangle$ on all bonds, lone pairs and unpaired electrons amounts to 13.38 e, in agreement with the electronegative character of the NO moiety. As indicated in Fig. 5, the C–N σ MPDs enhance the polarization toward the N center. The N–O σ MPD is smaller. The oxygen lone pair MPD dominates the O side of the molecule. The MPD relative to a pair of electrons can be associated with a π bond between N and O. This MPD is very mobile: similar and close optimal domains can be found with very similar probability values. This is a situation of 'multiple solution' probability domain already identified by Savin [24]; the physical multiplicity may reflect a situation in which several solutions can be obtained in the optimization of Ω for a given $v(\Omega_v)$ and will be the object of future analysis on MPDs method. Furthermore, the MPDs relative to a single electron for three representative PROXYL structures with different piramidalization degrees at the nitrogen atom have been computed and are reported in Fig. 6. The unpaired electron MPD reproduces the spatial description of spin density found in the case of a flat NO moiety. The single electron MPD has very small overlap with other domains: it inserts in the space left by the oxygen lone pairs and the N–O π domain. As the degree of pyramidalization increases, the population of this domain shifts clearly toward the oxygen center, while the residual probability at the nitrogen center still plays a crucial role in tuning the ESR observable.

The trends observed for a_N can be now put into a more general perspective by recalling that both direct and spin-polarization contributions to a_N are roughly proportional to the spin population in the singly occupied highest energy molecular orbital (SOMO) [4]. In the planar conformation (which we have seen does not necessarily correspond to a minimum on the PES), the only contribution to a_N is related to spin polarization, because the SOMO has a π nature. However, pyramidalization at the nitrogen center

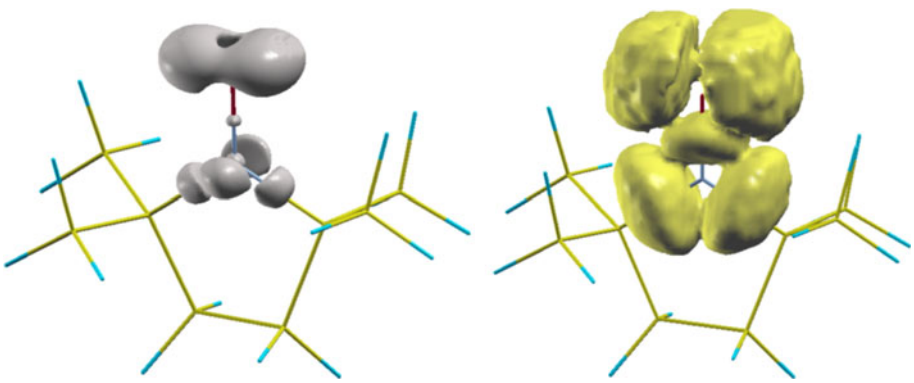

Fig. 5 *Left* ELF iso-surface of the NO moiety in the equilibrium structure; a ELF value of 0.83 has been chosen for the electron function. *Right* maximum probability domains relative to electron pairs associated with C–N σ bonds, N–O σ bond and oxygen lone pairs

Table 3 Results of MPD analysis for the equilibrium structure of PROXYL

Domain name	p_0	p_1	p_2	p_3	$\langle N \rangle$	Volume
C–N	0.04	0.23	**0.38**	0.24	2.12	13.3 (1.47)
N–O σ	0.07	0.27	**0.37**	0.21	1.99	7.6 (1.22)
O lone pair	0.04	0.24	**0.42**	0.23	2.04	22.2 (1.74)
N–O π	0.10	0.27	**0.32**	0.20	1.96	19.1 (1.66)
N–O unpaired	0.30	**0.39**	0.22	0.07	1.11	1.5 (0.72)

The probability p_v value for which the domain is optimized is highlighted in bold; the average number of electrons in Ω, $\langle N \rangle$ is reported for each domain. The volume of the domain is expressed in bohr^3; in brackets the radius (in bohr) of the equivalent sphere is also reported

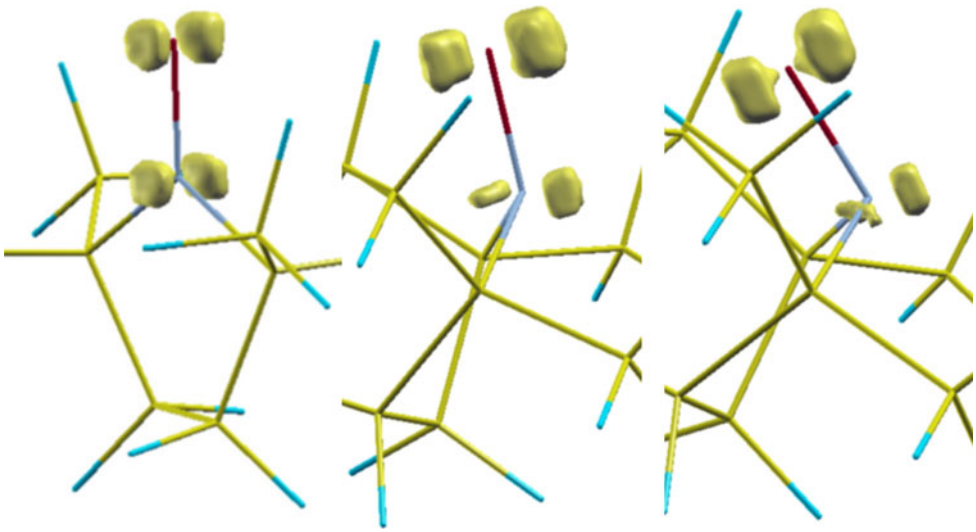

Fig. 6 Maximum probability domain relative to a single electron for three representative structures. *Left* equilibrium structure with an improper dihedral angle C–N–O–C equal to 180°. *Center* dihedral angle C–N–O–C equal to 136°. *Right* dihedral angle C–N–O–C equal to 118°

allows for the direct involvement of the nitrogen *s*-type orbital in the SOMO, leading to a large direct contribution to the Fermi contact term, which overcomes the spin-polarization term and determines the observed increase in a_N.

4 Concluding remarks

In the present account, we discussed two case studies by focusing our attention on the interplay of nuclear motions and solvation in tuning the electronic structure of molecules that are relevant for their spectroscopic properties and photophysical behavior.

For what concerns the 9-Me-Ade excited state decay, our results cannot be considered definitive since a fully reliable description of the vibronic coupling between L_a and $Sn\pi$ states would require a complete treatment of the explicit solute–solvent interactions and an accurate diabatization procedure. However, our analysis shows that the intramolecular vibrational motion at finite temperature significantly increases the mixing between L_a and $Sn\pi$,

which is larger than that found in the absolute ground state minimum at 0 K. On the other hand, we have shown that for 9-Me-Ade in solution in 50 % of the sampled geometries, the ratio between the less intense ($Sn\pi$ like) and most intense (L_a like) transition is smaller the 0.1, indicating a very weak coupling between the states. Since inclusion of solute–solvent hydrogen bonds is expected to increase the energy gap between the two diabatic states, our analysis casts some doubts on a significant involvement of the $Sn\pi$ state in the deactivation mechanism.

Regarding the results on ESR parameters of nitroxide spin probes, we have shown how considering only minimum-energy structures in the computation of a_N leads to predictions that are qualitatively unreliable and quantitatively far from the experimental counterparts, for example in the case of PROXYL. In the case of TEMPO, the agreement between static minimum-energy values and those obtained when dynamics is properly taken into account through AIMD average is caused by a fortuitous cancelation of effects. Evidently, this does not mean that neglecting molecular dynamics may represent in general a safe and reliable computational strategy.

In conclusion, the above examples highlight the relevance of a proper description, within a QM computational protocol, of two key factors, namely thermal averaging effects and the role of the chemical surroundings. Theoretical developments of multi-scale methods along these directions represent a significant step toward the challenging task of a direct comparison between experiments and simulations and promise to become a valuable tool for supporting the interpretation of ambiguous laboratory data and for driving the design and synthesis of innovative chemical systems.

Acknowledgments Financial support was provided by MIUR (PRIN 2008 and FIRB Futuro in Ricerca). The authors gratefully acknowledge the inspiration, guidance and support provided over the years by Professor Vincenzo Barone, and wish him a happy 60th birthday.

References

1. Barone V (ed) (2012) Computational strategies for spectroscopy: from small molecules to nano systems. Wiley, Hoboken
2. Parr RG, Yang W (1989) Density-functional theory of atoms and molecules. Oxford University Press, New York
3. Santoro F, Barone V (2010) Int J Quantum Chem 110:476
4. Improta R, Barone V (2004) Chem Rev 104:1231
5. Barone V (2005) J Chem Phys 122:014108
6. Leach AR (2001) Molecular modeling: principles and applications. Pearson Education, Harlow
7. Carr R, Parrinello M (1985) Phys Rev Lett 55:2471
8. Marx D, Hutter J (2000) Modern methods and algorithms of quantum chemistry, John von Neumann Institute for Computing, Julich, vol 1, chap. Ab initio molecular dynamics: theory and implementation. p 301
9. Crespo-Hernandez CE, Cohen B, Kohler B (2004) Chem Rev 104:1977
10. Middleton CT, de La Harpe K, Su C, Law YK, Crespo-Hernandez CE, Kohler B (2009) Annu Rev Phys Chem 60:13
11. Markovitsi D, Gustavsson T, Talbot F (2007) Photochem Photobiol Sci 6:717
12. Markovitsi D, Gustavsson T, Vayá I (2010) J Phys Chem Lett 1:3271
13. Gustavsson T, Improta R, Markovitsi D (2010) J Phys Chem Lett 1:2025
14. Hare PM, Crespo-Hernandez CE, Kohler B (2007) Proc Natl Acad Sci USA 104:435
15. Perun S, Sobolewski AL, Domcke W (2005) J Am Chem Soc 127:6257
16. Lu Y, Lan ZG, Thiel W (2011) Angew Chem Int Edit 50:6864
17. Berliner LJ (ed) (1998) Biological magnetic resonance, spin labeling in the next millennium, vol 14. Plenum Press, New York
18. Pavone M, Cimino P, Crescenzi O, Sillanpaa A, Barone V (2007) J Phys Chem B 111:8928
19. Pavone M, Sillanpaa A, Cimino P, Crescenzi O, Barone V (2006) J Phys Chem B 110:16189
20. Cimino P, Pavone M, Barone V (2007) J Phys Chem A 111:8482
21. Rinkevicius Z, Murugan NA, Kongsted J, Frecu B, Steindal AH, Agren H (2011) J Chem Theory Comput 7:3261
22. Houriez C, Ferre N, Masella M, Siri D (2008) J Chem Phys 128:244504
23. Pavone M, Biczysko M, Rega N, Barone V (2010) J Phys Chem B 114:11509
24. Causà M, Savin A (2011) J Phys Chem A 115:13139
25. Savin A (2002) In: Reviews of modern quantum chemistry: a celebration of the contributions of Robert G. Parr. World Scientific, Singapore, p 43
26. Becke A (1990) J Chem Phys 92:5397
27. Cancès E, Keriven R, Lodier F, Savin A (2004) Theor Chem Acc 111:373
28. Adamo C, Barone V (1999) J Chem Phys 110:6158
29. Levy M, Perdew JP (1993) Phys Rev B 48:11638
30. Lieb EH, Oxford S (1981) Int J Quantum Chem 19:427
31. Tomasi J, Persico M (1994) Chem Rev 94:2027
32. Tomasi J, Mennucci B, Cammi R (2005) Chem Rev 105:2999
33. Cossi M, Barone V (2001) J Chem Phys 115:4708
34. Schlegel HB, Millam JM, Iyengar SS, Voth GA, Daniels AD, Scuseria GE, Frisch MJ (2001) J Chem Phys 114:9758
35. Iyengar SS, Schlegel HB, Millam JM, Voth GA, Scuseria GE, Frisch MJ (2001) J Chem Phys 115:10291
36. Schlegel HB, Iyengar SS, Li X, Millam JM, Voth GA, Scuseria GE, Frisch MJ (2002) J Chem Phys 117:8694
37. Rega N, Iyengar SS, Voth GA, Schlegel HB, Vreven T, Frisch MJ (2004) J Phys Chem B 108:4210
38. Prendergast D, Grossman JC, Galli G (2005) J Chem Phys 123:014501
39. Lan ZG, Lu Y, Fabiano E, Thiel W (2011) Chem Phys Chem 12:1989
40. Barone V, Cimino P, Stendardo E (2008) J Chem Theor Acc 4:751
41. Barone V, Cimino P (2008) Chem Phys Lett 454:139
42. Barone V, Cimino P (2009) J Chem Theory Comput 5:192
43. Frisch MJ, Trucks GW, Schlegel HB, Scuseria GE, Robb MA, Cheeseman JR, Scalmani G, Barone V, Mennucci B, Petersson GA, Nakatsuji H, Caricato M, Li X, Hratchian HP, Izmaylov AF, Bloino J, Zheng G, Sonnenberg JL, Hada M, Ehara M, Toyota K, Fukuda R, Hasegawa J, Ishida M, Nakajima T, Honda Y, Kitao O, Nakai H, Vreven T, Montgomery JA Jr, Peralta JE, Ogliaro F, Bearpark M, Heyd JJ, Brothers E, Kudin KN, Staroverov VN, Kobayashi R, Normand J, Raghavachari K, Rendell A, Burant JC, Iyengar SS, Tomasi J, Cossi M, Rega N, Millam JM, Klene M,

Knox JE, Cross JB, Bakken V, Adamo C, Jaramillo J, Gomperts R, Stratmann RE, Yazyev O, Austin AJ, Cammi R, Pomelli C, Ochterski JW, Martin RL, Morokuma K, Zakrzewski VG, Voth GA, Salvador P, Dannenberg JJ, Dapprich S, Daniels AD, Farkas, Foresman JB, Ortiz JV, Cioslowski J, Fox DJ. Gaussian 09 Revision A.2. Gaussian Inc. Wallingford CT 2009
44. Dovesi R, Saunders VR, Orlando R, Zicovich-Wilson CM, Pascale F, Civalleri B, Doll K, Bush IJ, DArco P, Lunell M. Crystal 2009 user manual. Turin University 2009
45. Pecourt JML, Peon J, Kohler B (2001) J Am Chem Soc 123:10370
46. Gustavsson T, Sharonov A, Onidas D, Markovitsi D (2002) Chem Phys Lett 356:49
47. Ullrich S, Schultz T, Zgierski MZ, Stolow A (2004) J Am Chem Soc 126:2262
48. Bisgaard CZ, Satzger H, Ullrich S, Stolow A (2009) Chem Phys Chem 10:101
49. Conti I, Garavelli M, Orlandi G (2009) J Am Chem Soc 131:16108
50. Santoro F, Barone V, Improta R (2007) Proc Natl Acad Sci USA 104:9931
51. Improta R, Barone V (2008) Theor Cheom Acc 120:491
52. Serrano-Andres L, Merchan M, Borin AC (2006) Proc Natl Acad Sci USA 103:8691
53. Serrano-Andres L, Merchan M, Borin AC (2006) Chem Eur J 12:6559
54. Fabiano E, Thiel W (2008) J Phys Chem A 112:6859
55. Santoro F, Barone V, Gustavsson T, Improta R (2006) J Am Chem Soc 128:16312
56. Improta R, Barone V, Santoro F (2007) Angew Chem Int Edit 46:405
57. Santoro F, Lami A, Improta R, Barone V (2007) J Chem Phys 126:184102
58. Keana JFW, Lee TD, Bernard EM (1976) J Am Chem Soc 98:3025
59. Knauer BR, Napier JJ (1976) J Am Chem Soc 91:4395
60. Onidas D, Markovitsi D, Marguet S, Sharonov A, Gustavsson T (2002) J Phys Chem B 106:11367